

Layer-dependent activity in human prefrontal cortex during working memory

Emily S. Finn^{1*}, Laurentius Huber^{1,2}, David C. Jangraw¹, Peter J. Molfese¹ and Peter A. Bandettini¹

Working memory involves storing and/or manipulating previously encoded information over a short-term delay period, which is typically followed by a behavioral response based on the remembered information. Although working memory tasks often engage dorsolateral prefrontal cortex, few studies have investigated whether their subprocesses are localized to different cortical depths in this region, and none have done so in humans. Here we use high-resolution functional MRI to interrogate the layer specificity of neural activity during different periods of a delayed-response task in dorsolateral prefrontal cortex. We detect activity time courses that follow the hypothesized patterns: namely, superficial layers are preferentially active during the delay period, specifically in trials requiring manipulation (rather than mere maintenance) of information held in working memory, and deeper layers are preferentially active during the response. Results demonstrate that layer-specific functional MRI can be used in higher-order brain regions to noninvasively map cognitive processing in humans.

Working memory (WM) is the highly evolved mental capacity to store and manipulate information for short-term use. It is often probed with delayed-response tasks that require encoding a stimulus, sustaining a representation of the stimulus over a delay, and finally making a memory-guided behavioral response.

The dorsolateral prefrontal cortex (dlPFC) has been linked to WM processes in both humans and nonhuman primates^{1–4}. Like much of the cerebral cortex, dlPFC gray matter is organized into layers with distinct cytoarchitecture, connectivity and function. Early electrophysiological work in nonhuman primates suggested that in delayed-response tasks, different task periods are preferentially associated with activity in different cortical layers^{5,6}. Specifically, delay-period activity is thought to be driven by recurrently connected networks of pyramidal cells in layer III³, whereas response-related activity takes place predominantly in layer V⁷. Two recent studies in macaques, which overcame the challenge of separating activity recorded from distinct cortical layers, provide direct evidence for this dissociation^{8,9}.

However, it remains unclear to what extent dlPFC exhibits homologous function between monkeys and humans. Although dlPFC often appears active during WM tasks in human functional MRI (fMRI) studies, human dlPFC may not be strictly necessary for mere maintenance of information—that is, for sustaining the representation of a stimulus ‘as-is’ without performing further operations on it. Instead, dlPFC may be necessary only when the task calls for rule-based manipulation of information stored in WM, for example, when items must be reordered or transformed in some other way. Indeed, disrupting dlPFC activity with lesions^{10,11} or repetitive transcranial magnetic stimulation¹² impairs manipulation but leaves maintenance largely intact.

To the extent that human dlPFC is specialized for manipulation rather than pure maintenance, the laminar specificity of these operations is unknown. Following an evolutionary progression, we hypothesize that manipulation in humans might recruit the same local recurrent excitatory networks of layer III pyramidal cells as

maintenance does in nonhuman primates. This hypothesis is also supported by converging evidence from schizophrenia, which is associated with reduced dendritic spine density specifically in dlPFC layer III neurons^{13,14} as well as behavioral deficits in manipulation (over and above maintenance)¹⁵. However, activity involved in response selection and action initiation may take place predominantly in infragranular layers, as has been observed in nonhuman primates^{9,16,17}. To date there is no empirical evidence for such a dissociation in humans, largely because conventional neuroimaging techniques lack the sensitivity and specificity to resolve cortical layers.

Recent methodological advances in fMRI, including higher field strengths (that is, 7 Tesla and above) combined with innovations in pulse sequences and contrast mechanisms, now allow for non-invasive, reliable measurements of cortical depth-dependent activity in humans. These advances have enabled layer-specific imaging in several primary cortices, including the visual^{18–20}, auditory²¹ and motor²² cortices. (Note that in the context of fMRI, the term ‘layer’ refers to estimates of different cortical depths, not necessarily to cortical layers as defined cytoarchitecturally.) Although simulations suggest that fMRI should in principle be able to resolve laminar differences in more complex tasks²³, it is still unclear if these techniques are sensitive and robust enough to be applied outside primary cortices.

Here, by further developing layer-fMRI methods to move beyond unimodal cortex²² into higher-order areas, we provide evidence for cortical depth-dependent processing during a sophisticated cognitive task in one of the most highly evolved regions of human association cortex. Specifically, we use simultaneously acquired blood oxygen level-dependent (BOLD) and cerebral blood volume (CBV) images of human dlPFC during a working memory task to show that during the delay period, manipulation evokes greater activity than maintenance, specifically in superficial layers, whereas during the response period, activity is localized to deeper layers. These results deepen our understanding of the laminar specificity of WM-based operations in humans and demonstrate the promise of high-resolution fMRI for mapping cognitive cortical circuitry at the mesoscale.

¹Section on Functional Imaging Methods, Laboratory of Brain and Cognition, National Institute of Mental Health, Bethesda, Maryland, USA. ²Present address: MR-Methods Group, Maastricht Brain Imaging Center, Department of Cognitive Neuroscience, Faculty of Psychology and Neuroscience, Maastricht University, Maastricht, The Netherlands. *e-mail: emily.finn@nih.gov

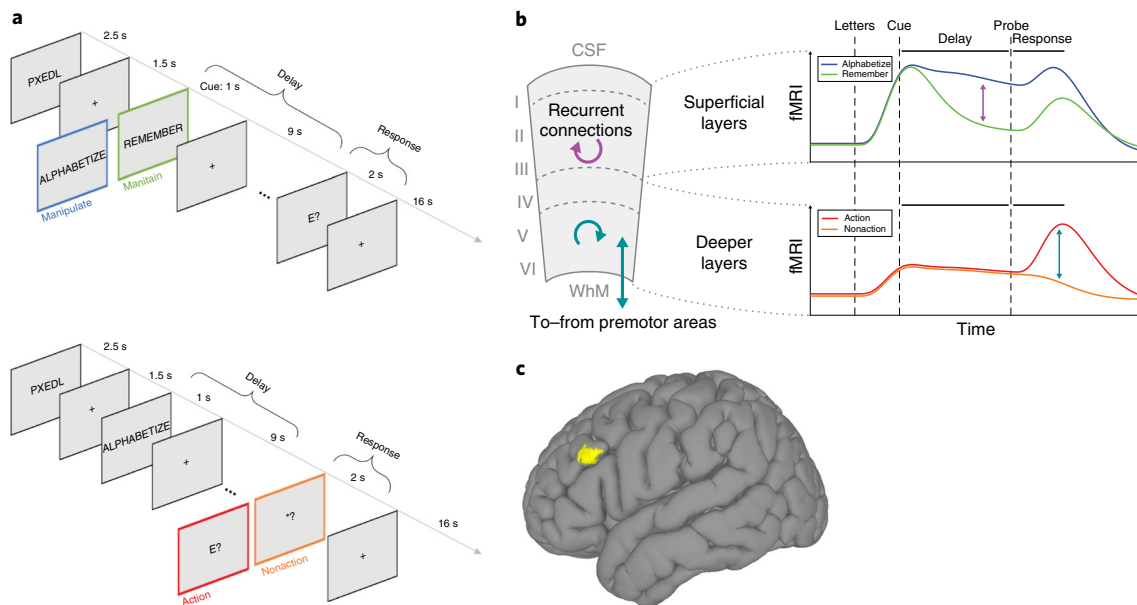


Fig. 1 | Task, hypothesis and region of interest. **a**, Trial structure. Top: first trial type, contrasting manipulation and maintenance during the delay period. Participants see a string of five random letters (for example, 'PXEDL'), then a cue instructing them to either rearrange the letters in alphabetical order ('ALPHABETIZE', manipulation condition) or to simply remember them in their original order ('REMEMBER', maintenance condition) over the course of a delay period, during which they see only a fixation cross. Finally, a probe letter comes onscreen (for example, 'E?'), and participants make a response to indicate the alphabetical or ordinal position of the probed letter. Bottom: second trial type, contrasting action and nonaction during the response period. These trials are identical to the first until the response period, at which point subjects see either a true probe requiring a button press (for example, 'E?', action condition) or a dummy probe (that is, "?", nonaction condition), which indicates that no response is required and that they can forget the information associated with that trial. Colored frames are for schematic purposes only and were not seen by participants. **b**, Schematic of hypothesis. We hypothesized that (i) in superficial layers, manipulation trials would evoke more activity than maintenance trials specifically during the delay period due to recurrent excitation in layer III (purple arrows), and (ii) in deeper layers, action trials would evoke more activity than nonaction trials due to action-selection and/or motor-related functions in layer V (teal arrows). **c**, Macroscale location of left dlPFC region of interest (MNI coordinates for center of mass: $(x = +49, y = -21, z = +23)$, computed via group analysis of whole-brain functional localizer data (resulting in cluster displayed at voxelwise $P < 0.01$). For single-subject layer ROIs, see Supplementary Fig. 3.

Results

Task paradigm. To test our hypotheses about layer-dependent activity during WM, we used a well-validated task paradigm that dissociates maintenance from manipulation during the delay period²⁴ and added a second contrast to separate action from nonaction during the response period. See Fig. 1a for a schematic of the task. All trials are matched for sensory input, with the only difference being the nature of the mental activity during the delay for the first contrast or the presence or absence of action selection and execution during the response period for the second contrast. (Note that an action-related signal can also be isolated from the first contrast by examining activity at the time of the response compared to all other time points; we exploit this in a second acquisition protocol described further below.)

Thus, the main paradigm followed a $2 \times 2 \times 2$ design, with trial type (manipulation/maintenance versus action/nonaction), period (delay versus response) and cortical depth (superficial versus deep) as the three factors. We hypothesized a triple dissociation between trial type, period and cortical depth, such that (1) superficial layers would respond more strongly during the delay period of manipulation trials (as compared to the delay period of maintenance trials) and (2) deeper layers would respond more strongly during the response period of action trials (as compared to the response period of nonaction trials). See Fig. 1b for a schematic of the hypothesis. The strength of this experimental design is that we control for each layer's time course of activity primarily by observing the same layer in a different condition, rather than directly comparing activity levels across layers; this design avoids measurement biases associated with different cortical depths.

Data acquisition. Functional data are from $n = 15$ unique subjects scanned in a combined total of 20 imaging sessions. During each high-resolution functional run, we simultaneously measured changes in CBV and BOLD signal, using the SS-SI-vascular space occupancy (VASO) method²⁵ with a three-dimensional echo-planar imaging (3D-EPI) readout²⁶ on a 7-T scanner. This method has been implemented to successfully demonstrate layer-specific activity in human motor cortex with good sensitivity and specificity²². The conventional BOLD signal has poor spatial specificity at high resolutions, since it tends to be dominated by large veins at the pial surface and depends on nonlinear interactions between physiological variables that can differ across cortical depths, making it difficult to quantitate. VASO, although it has a lower contrast to noise ratio, is a more quantitative measurement that is less biased toward superficial depths. In short, BOLD is more sensitive, while VASO is more specific.

We used two different acquisition protocols over the course of the study. The first had a nominal voxel resolution of $0.9 \times 0.9 \times 1.1 \text{ mm}^3$ (referred to as the 'axial [readout] protocol'). These data were used to quantitatively compare activity time courses across two distinct cortical depths (superficial versus deep) at the group level. Later, we introduced a second, higher-resolution protocol with nominal voxel resolution of $0.76 \times 0.76 \times 0.99 \text{ mm}^3$ (referred to as the 'sagittal [readout] protocol'). These data were used to visualize activity across different layers in individual subjects. For both protocols, the field of view was not the whole brain but rather a slab centered on a region of interest within left dlPFC that was identified via an online functional localizer conducted at the start of each imaging session.

(Due to restrictions on its MRI sequence parameter space and the need to apply a slab-selective inversion pulse, VASO is currently limited in the spatial coverage that can be achieved at these resolutions.) See Methods and Supplementary Fig. 1 for further details of our data acquisition and analysis pipeline.

Location of region of interest. Prefrontal cortex is large and quite variable across individuals in its structure and functional anatomy. Unlike other cortical landmarks, such as the ‘hand knob’ of the primary motor cortex, functional subdivisions of prefrontal cortex are difficult to pinpoint in individual subjects by macroscale anatomical features. Therefore, regions of interest (ROIs) were selected for each subject on the basis of an online functional localizer conducted just before the experimental task runs (see Methods). Given that imaging parameters could only be optimized for one hemisphere at a time, we focused on left dlPFC in all subjects, considering previous reports as well as our own pilot experiments indicating that this task more strongly engages the left over the right hemisphere. (Because our stimuli, letters, were verbal in nature, this lateralization may be due in part to a left-hemisphere dominance for language.)

Despite the variance in prefrontal cortex size and anatomy across subjects, the ROI location was highly consistent with respect to the subject-specific cortical folding structure that was visible in EPI space. In all subjects, the ROI was located in the ventral portion of the middle frontal gyrus corresponding approximately to Brodmann area 9/46 (ref. 27). To ensure that our ROI selection procedure was robust, we conducted test–retest scans separated by several weeks on two subjects. Results showed good overlap between ROIs derived from independent experimental sessions (Supplementary Fig. 2), indicating that the functional region in question can be reliably localized within subjects. Figure 1c shows the average ROI location across subjects computed from the whole-brain functional localizer (although note that this figure is a post hoc visualization only; all analyses of the high-resolution experimental data were conducted in single-subject space to preserve spatial specificity). See Supplementary Videos 1–6 for slice-by-slice visualizations of the selected ROI in six individual subjects.

For each subject, two layers, superficial and deep, were each drawn manually within the selected ROI (see Supplementary Fig. 3 for layer masks for all subjects scanned using the axial readout protocol). To better specify the position of our ‘superficial’ and ‘deep’ layers with respect to cortical laminae defined cytoarchitecturally, we compared all available MRI-based anatomical contrasts with an existing histological image (Supplementary Fig. 4). The boundary between our superficial and deeper layers fell approximately between layer III and layer IV.

Task performance. Subjects performed well on the task (overall mean accuracy = 0.82; s.d. = 0.13; range, 0.59–0.97; note that chance is approximately 0.2), including both manipulation trials (mean (s.d.), 0.79 (0.13); range, 0.54–0.96) and maintenance trials (mean (s.d.), 0.88 (0.15); range, 0.53–1.0). Subjects were less accurate on manipulation than maintenance trials (paired t -test, $t_{14} = -3.28$, $P = 0.01$), which is expected given previous reports using this task²⁴.

Overall mean reaction time was 2.37 s (s.d., 1.24; range, 1.05–5.17). Crucially, there was no difference between mean reaction time on manipulation versus maintenance trials (paired t -test, $t_{14} = 1.29$, $P = 0.22$). It is therefore unlikely that conditions differ in latency of peak response-related activity, allowing us to directly compare time courses without deconvolution.

Activity time courses. Using data from 15 experimental sessions ($n = 13$ unique subjects) scanned with the axial protocol, we observed layer-dependent activity time courses that followed the hypothesized patterns: in superficial layers, activity was higher in

manipulation than in maintenance trials during the delay period, and in deeper layers, activity was higher in action than in nonaction trials during the response period. These patterns were visible in both VASO and BOLD (Fig. 2, Supplementary Fig. 5). Below we summarize characteristics of these depth-dependent time courses during the two main periods of interest, delay and response.

Delay-related activity. In superficial layers (Fig. 2a, top row), delay-period activity was uniformly high during manipulation trials. This was evident in trials ‘alpha’, ‘action’ and ‘nonaction’ trials (recall that both action and nonaction trials called for alphabetizing, and they were indistinguishable from one another until the probe appears). Superficial delay-related activity was higher during manipulation than maintenance, although results from the more sensitive BOLD contrast indicated that maintenance alone was also sufficient to evoke above-baseline activity (Supplementary Fig. 5). In addition to the group-level results shown in Fig. 2, this effect was clearly visible in single-subject data (Supplementary Fig. 6).

In contrast to superficial layers, deeper layers were markedly less active during the delay period (Fig. 2a, bottom row; although note that the BOLD data in particular suggested that their activity was still slightly above baseline during this period, Supplementary Fig. 5). Thus, it seems that delay-related activity occurs predominantly, if not exclusively, in superficial layers, and particularly when task demands call for manipulation of information stored in WM rather than mere maintenance.

Response-related activity. During the response period, we observed the opposite pattern: activity in the deeper layers was high, but only in trials requiring an action. Deeper-layer activity peaked at the time of the response, which was expected approximately 6–7 s after the probe came onscreen (reflecting behavioral and hemodynamic delay). As expected, this peak was present in action but not nonaction trials (Fig. 2a, bottom right). Again, this effect was also visible in most individual subjects (Supplementary Fig. 7).

As for superficial layers, their activity was, if anything, suppressed at the response peak in both trial types (Fig. 2a, top right). This confirmed our prediction that the response period would be preferentially associated with activity in deeper cortical layers.

These same patterns were visible to some degree in the BOLD contrast (Supplementary Fig. 5), although the strong superficial bias of BOLD makes it difficult to draw firm conclusions from these data. (For example, the apparent difference between action and nonaction trials in superficial layers visible in Supplementary Fig. 5a, top right, is likely an artifact of draining veins from the deeper layers, since this difference is not present at all in the VASO data shown in Fig. 2a, top right.) Due to the higher spatial specificity and more quantitative nature of VASO, we performed all statistical comparisons using this contrast as described in the following section.

Quantification of differential activity. To quantitatively compare activity within cortical depths, we performed a series of two-way, repeated-measures analyses of variance (ANOVAs) using representative signals from each trial type during each trial period. In each ANOVA, the two factors were trial type (either ‘alphabetize’ and ‘remember’ or ‘action’ and ‘nonaction’) and trial period (delay and response), with subject as the repeated measure.

For superficial layers, we found a significant interaction between trial type (manipulation versus maintenance or ‘alphabetize’ versus ‘remember’) and trial period ($F(1,14) = 34.7$, $P = 7.7 \times 10^{-5}$), such that activity was higher in manipulation trials but only during the delay period (Fig. 2b, top left). As expected, the contrast between the second condition pair (action versus nonaction) revealed a main effect of period ($F(1,14) = 123.0$, $P = 2.6 \times 10^{-8}$), such that activity

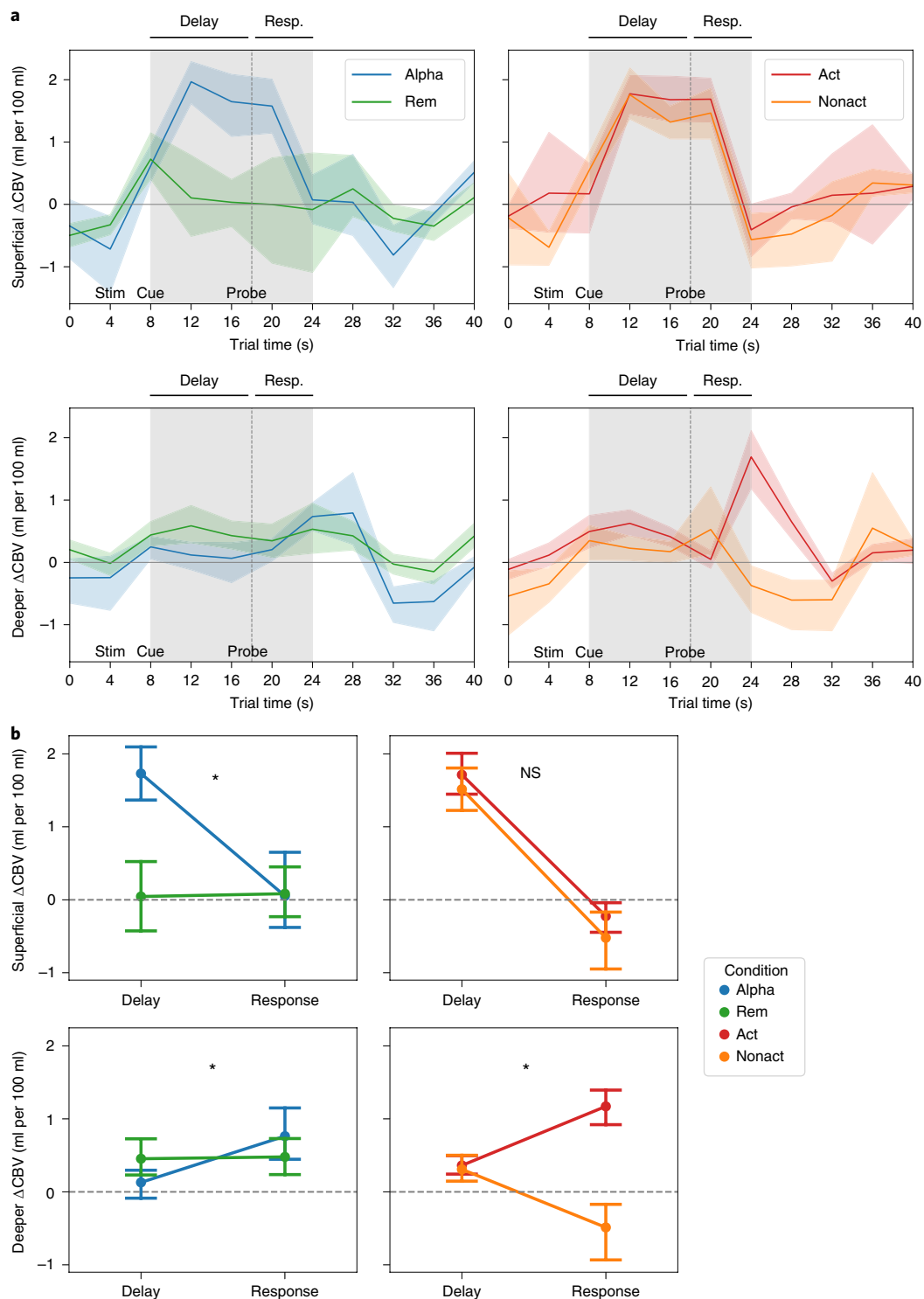


Fig. 2 | Different trial types evoke distinct spatiotemporal patterns of activity. **a**, Left: mean VASO signal change (in units of ml per 100 ml CBV) in superficial layers (top) and deeper layers (bottom) for the first contrast, manipulation trials ('alpha') versus maintenance trials ('rem'). Resp., response. Right: mean VASO signal change in superficial layers (top) and deeper layers (bottom) for the second contrast, action trials ('act') versus nonaction trials ('nonact'). Lines represent mean and shaded area represents 95% confidence intervals for the mean (determined via bootstrapping with 1,000 iterations) across $n = 15$ sessions (13 unique subjects). See Supplementary Figs. 6 and 7 for single-subject time courses and Supplementary Fig. 5a for mean BOLD time courses. **b**, Two-way ANOVA with the factors trial period (delay versus response) and trial type (either manipulation ('alpha') versus maintenance ('rem') or action versus nonaction) in superficial (top) and deeper (bottom) layers. Panels as in **a**. Dots represent mean and error bars reflect 95% confidence intervals for the mean. *Interaction significant at $P < 0.01$ ($P = 7.7 \times 10^{-5}$ for the superficial alphabetize-versus-remember contrast, top left; $P = 0.002$ for the deeper action-versus-nonaction contrast, bottom right; $P = 0.004$ for the deeper alphabetize-versus-remember contrast, bottom left); NS, interaction not significant ($P = 0.68$ for superficial action-versus-nonaction contrast, top right).

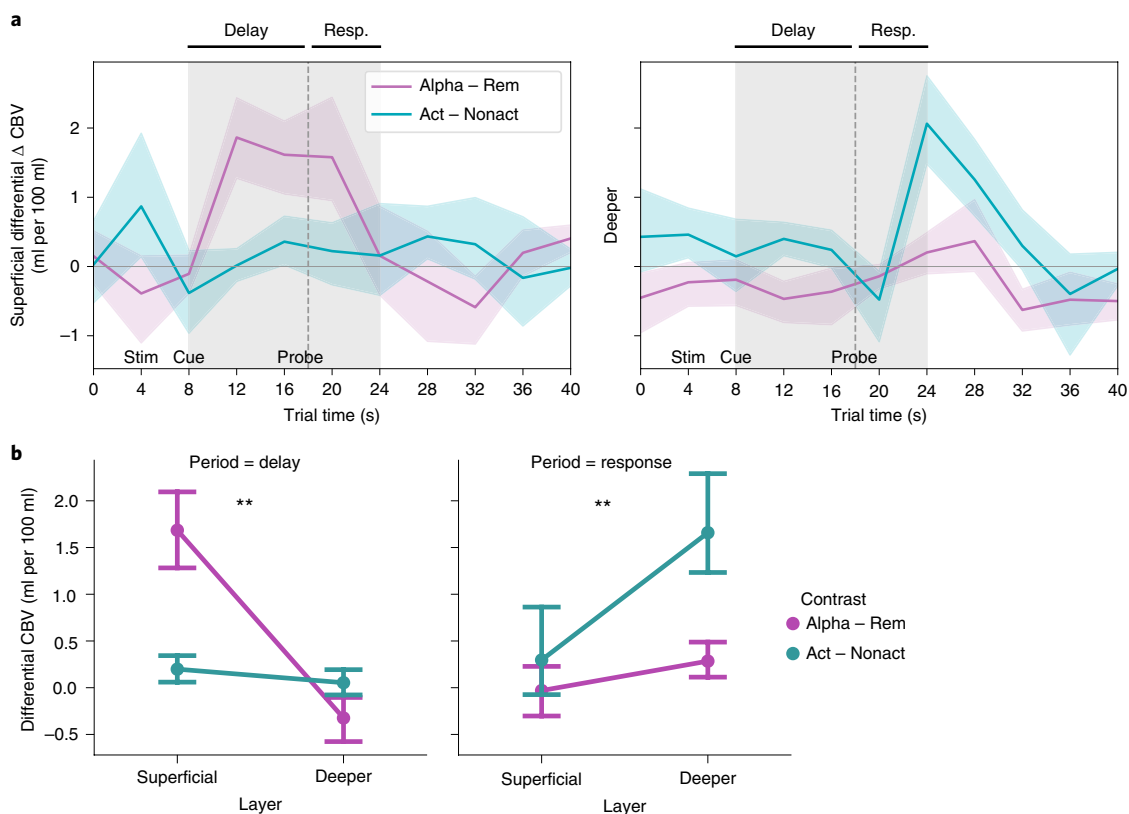


Fig. 3 | Activity contrasts across layers and conditions of interest. **a**, Left: superficial-layer VASO activity during maintenance ('rem') trials subtracted from activity during manipulation ('alpha') trials (purple line), and VASO activity during nonaction ('nonact') trials subtracted from activity during action ('act') trials (teal line). The largest difference can be seen for the alpha - rem contrast during the delay period. Right: deeper-layer VASO activity subtractions (colors as in left panel). The largest difference can be seen for the act - nonact contrast during the response period. Lines represent mean and shaded area represents 95% confidence intervals for the mean (determined via bootstrapping with 1,000 iterations) across $n=15$ sessions (13 unique subjects; same data as in Fig. 2). See Supplementary Fig. 5b for subtractions based on mean BOLD activity time courses. **b**, Two-way ANOVA with factor layer (superficial versus deeper) and contrast (manipulation-maintenance ('alpha - rem', purple lines) versus action - nonaction (teal lines)) for each trial period (delay and response). Dots represent mean and error bars reflect 95% confidence intervals for the mean (determined via bootstrapping with 1,000 iterations) across $n=15$ sessions (13 unique subjects). **Interaction significant at $P < 0.001$ ($P = 6.9 \times 10^{-6}$ and $P = 3.0 \times 10^{-4}$ for the delay period (left) and response period (right), respectively).

was higher during the delay than during the response, but no interaction between period and trial type ($F(1,14) = 0.19$, $P = 0.68$; Fig. 2b, top right).

For deeper layers, as predicted, we found the opposite pattern of results. There was a significant interaction between trial type (action versus nonaction) and trial period ($F(1,14) = 26.0$, $P = 0.002$), such that activity was higher in action trials during the response (Fig. 2b, bottom right). The contrast between the manipulation and maintenance conditions indicated an interaction such that activity was higher during the response than during the delay but only in manipulation trials ($F(1,14) = 13.4$, $P = 0.004$; Fig. 2b, bottom left).

Another way to assess relevant differences is to subtract the average time course within each depth between the trial types of interest. Results indicated that for superficial layers, the difference between manipulation and maintenance peaked during the delay period (Fig. 3a, left, and Supplementary Fig. 5b, top), whereas for deeper layers, the difference between action and nonaction trials peaked at the time of the response (Fig. 3a, right, and Supplementary Fig. 5b, bottom).

As a final quantification step, we statistically compared these differential activity levels by performing ANOVAs on representative signals from each period (delay and response) in each differential time course (manipulation-maintenance and action-nonaction),

again with subject as the repeated measure (Fig. 3b). Although directly comparing superficial and deeper layers should be done with caution because results can be biased by cross-depth differences in baselines, scale factors and vascular cross-talk, in this case we use a difference-of-differences approach that helps mitigate some of these concerns. Results confirm that during both trial periods, there is an interaction between layer and condition pair such that during the delay period, superficial layers are more sensitive to the manipulation-maintenance contrast ($F(1,14) = 92.7$, $P = 6.9 \times 10^{-6}$; Fig. 3b, left), whereas during the response period, deeper layers are more sensitive to the action-nonaction contrast ($F(1,14) = 30.5$, $P = 0.0003$; Fig. 3b, right).

Visualization of depth-dependent activity. To better visualize the depth-dependent distribution of activity associated with different periods within the trial, we used a second, higher-resolution imaging protocol in which the field of view was a sagittal slab centered on dlPFC with in-plane resolution of 0.76×0.76 mm². In these experiments, the task consisted exclusively of manipulation/maintenance trials, all requiring an active response (that is, the first contrast type shown in Fig. 1a, top). Functional signals during manipulation and maintenance trials were investigated across cortical depths.

We detected layer-dependent activity in all individual subjects imaged with this protocol ($n = 5$; Fig. 4). Manipulation evoked more

activity than maintenance predominantly in superficial layers (green stripes), whereas signal associated with response (as compared to baseline; red stripes) was predominantly localized to deeper layers. These patterns were visible in both the BOLD (Fig. 4a) and VASO (Fig. 4b) contrasts (although note the different thresholds). Layer ROIs for each subject are shown in Fig. 4c. A discussion of the observed variance in functional response across the cortical surface (that is, across columns) is given in Supplementary Fig. 8.

Discussion

Although working memory has been known to engage dlPFC for decades, the degree to which its subprocesses were layer specific had been hypothesized³ but had been demonstrated only a handful of times in nonhuman primates^{8,9}. Furthermore, the extent of functional homology in this region between humans and nonhuman primates was unclear. Here we interrogated layer-specific functionality directly and noninvasively in humans, shedding new light on the laminar specificity of WM processes in dlPFC. By developing and optimizing state-of-the-art techniques in high-resolution fMRI for cognitive brain areas and using a task design for which we had hypotheses about the location, magnitude and timing of neural activity, we were able to detect time courses at different cortical depths that followed the expected patterns. Namely, we observed delay-related manipulation activity that was predominantly localized to superficial layers and response-related activity that was predominantly localized to deeper layers.

We interpret the observed laminar specificity of distinct working memory processes in light of what is known about underlying neural circuitry. First, superficial activity during the delay period may at least partially reflect recurrent excitatory connections. Although in early parts of the cortical hierarchy, superficial layers give rise to feedforward connections, at the highest levels (that is, PFC), laminar projections become more complex. Layer III expands and is the focus of extensive local, recurrent excitatory connections²⁸, as well as long-range recurrent connections with other regions that may be involved in storing items in working memory, for example, parietal association cortex^{7,29}. Recurrent excitation among these cells is a feature of their unique molecular profile, notably their preferential expression of *N*-methyl-D-aspartate receptors and specifically the NR2B subunit, whose slower kinetics allow for persistent firing over long delays; this feature has been predicted by computational models³⁰ and confirmed experimentally in nonhuman primates³¹. Although our findings suggest that superficial layers are active specifically when the task calls for manipulating and not just storing information, with our current task design, we cannot fully rule out the possibility that superficial-layer activity depends somewhat on task difficulty or engagement more generally. In future work, designs that parametrically vary load under both manipulation and maintenance conditions will help define the precise functional role of superficial-layer cells in dlPFC.

Second, response-period activity in deeper layers likely reflects functions related to response selection, action execution or both. In our task paradigm, a response could not be selected until the probe appeared onscreen. This is in keeping with typical delayed-response paradigms used in human neuroimaging but different from those used with nonhuman primates, which are based on oculomotor responses to a single remembered item, meaning the animal can predict the upcoming response during the delay period. Human neuroimaging studies suggest a role for dlPFC in selecting and planning an appropriate task response^{32–34}, even in the absence of a working memory requirement³⁵; this activity scales with factors affecting response selection even while eventual motor output is held constant³⁶, seeming to indicate response selection as the dominant process taking place in dlPFC. However, nonhuman primate electrophysiological studies, most notably those featuring laminar specificity^{8,9}, report deeper-layer activity that appears to track action

execution (that is, saccades) more directly. This activity might reflect one or a number of processes related to motor execution, such as initiating an action, suppressing prepotent responses or a feedback mechanism such as corollary discharge. Although dlPFC does not project directly to primary motor cortex (M1), it may influence motor behavior polysynaptically via higher-order cortical motor areas^{37,38} or the striatum^{39,40}. Like most delayed-response human fMRI paradigms, our task timing and temporal resolution do not allow us to separate response selection from action initiation itself, meaning future work will be necessary to dissociate these two processes and the extent to which they account for the layer-specific response profiles observed here.

Of note, schizophrenia is associated with altered genetics⁷, morphology^{13,14} and function⁴¹ in this dlPFC circuitry. Decreased delay-related activity in superficial layers, as well as disinhibition in deeper layers, may underlie the deficits in working memory and other cognitive functions seen in these patients. We expect that future studies using layer fMRI in populations with or at risk for schizophrenia will shed new light on the spatiotemporal dynamics of cognitive dysfunction in this illness.

From a methodological perspective, here we used advanced contrast mechanisms and balanced task design to offset differences in vascular physiology across cortical depths, which can introduce substantial biases and limit the interpretability of layer fMRI⁴². In contrast to gradient-echo BOLD, CBV-weighted fMRI signal acquired with VASO allows appropriate separation of microvascular responses at a layer-dependent level^{43,44}. We avoid biases of different hemodynamic response functions across cortical depths^{45,46} by refraining from using general linear model deconvolution with pre-defined hemodynamic response functions, and by restricting our interpretation to quantitative signal differences that are obtained at the same latency within identical task blocks. Additionally, we collected conventional gradient-echo BOLD fMRI concomitantly with VASO data. The near-simultaneous acquisition of BOLD and VASO data allowed us to obtain a clean BOLD-corrected, CBV-weighted VASO signal. The higher sensitivity of BOLD compared to VASO was helpful in selecting the correct ROI, whereas the higher spatial specificity of VASO was helpful for interpreting signal across cortical depths.

These methodological advances have exciting implications for noninvasive, in vivo mapping of input–output and feedforward–feedback connections in the human neocortex. Outstanding challenges include expanding spatial coverage without sacrificing resolution, which would allow for functional connectivity analyses to infer information flow between far-flung cortical areas. For example, simultaneous imaging of dlPFC, premotor and primary motor cortices would help characterize interregion interactions during response selection and execution, and expanding coverage to parietal and sensory areas as well as neighboring prefrontal areas would help characterize interactions that support stimulus perception, information storage and manipulation during the encoding and delay periods.

Looking beyond working memory, these tools provide a starting point for mapping layer-specific connections within high-order association cortex and between high-order and unimodal cortex, in the context of cognitive neuroscience. Many influential theories of brain function that posit top-down and bottom-up signals with origins and destinations in distinct cortical layers—for example, predictive coding and related frameworks—may now be directly tested in humans⁴⁷. This opens the door to investigating computational mechanisms behind any number of neuropsychological phenomena, such as selective attention, hallucinations and delusions, and even consciousness itself, to name a few⁴⁸. We expect that the ever-advancing tools of high-resolution fMRI will ultimately transform our understanding of cognition in the awake, behaving human brain.

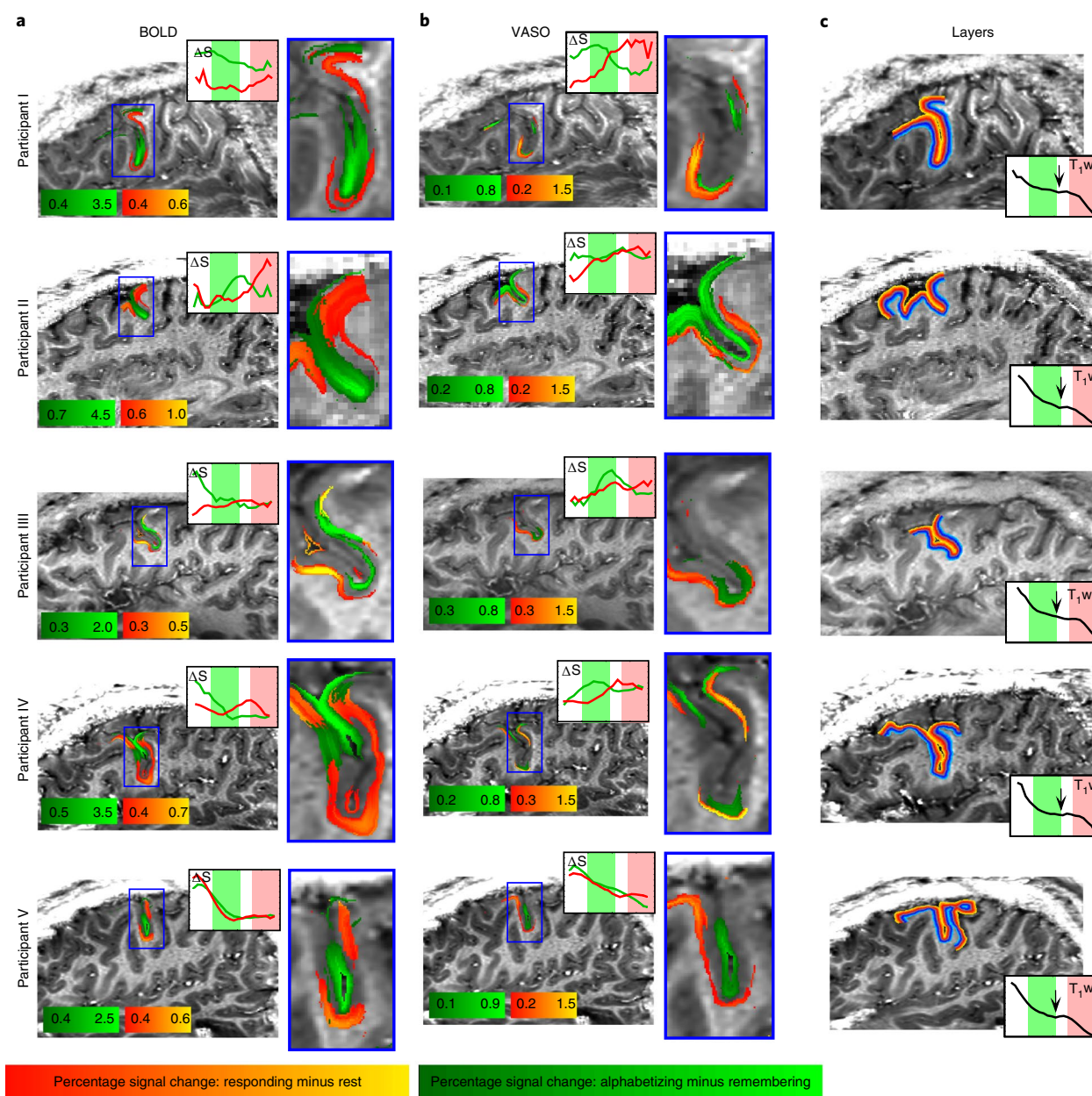


Fig. 4 | Single-subject, layer-dependent activity profiles. Results from five subjects scanned with the sagittal protocol. **a,b**, Activity is shown in both functional contrasts, BOLD (**a**) and VASO (**b**). Signal changes for delay and response periods are smoothed within layers. No smoothing was applied across layers. Note the different color scales for BOLD and VASO. Color intensity indicates percentage signal change. Red/orange reflects increased signal during the response period compared to baseline (intertrial interval). Green represents increased signal during the delay period for manipulation compared to maintenance trials. Inset line graphs show the corresponding layer activity profiles plotted across cortical depth, from superficial (left) to deep (right) as in the average activity profile plots shown in the bottom row. In VASO insets (**b**), note that the red line is always above the green line in the deeper layers (red shading), whereas the green line is always above the red line in the superficial layers (green shading), meaning that the task used here engages the superficial and deeper layers differently. This finding is consistent across subjects. **c**, Estimates of layers (cortical depths) for each subject. Insets in **c** are subject-specific layer profile distributions of the T_1 -weighted (T_{1w}) EPI signal, from superficial (left) to deep (right). The black arrow indicates the location of a myelin-related signal dip, which can be taken as a landmark for the transition region between cytoarchitectonic layer III and layer V (see Supplementary Fig. 4). Error bars in average profiles (bottom row) reflect s.e.m. across subjects.

Online content

Any methods, additional references, Nature Research reporting summaries, source data, statements of code and data availability and associated accession codes are available at <https://doi.org/10.1038/s41593-019-0487-z>.

Received: 25 April 2019; Accepted: 5 August 2019;
Published online: 23 September 2019

References

- Courtney, S. M., Ungerleider, L. G., Keil, K. & Haxby, J. V. Transient and sustained activity in a distributed neural system for human working memory. *Nature* **386**, 608 (1997).
- Courtney, S. M., Petit, L., Maisog, J. M., Ungerleider, L. G. & Haxby, J. V. An area specialized for spatial working memory in human frontal cortex. *Science* **279**, 1347–1351 (1998).
- Goldman-Rakic, P. Cellular basis of working memory. *Neuron* **14**, 477–485 (1995).
- D'Esposito, M. et al. The neural basis of the central executive system of working memory. *Nature* **378**, 279 (1995).
- Sawaguchi, T., Matsumura, M. & Kubota, K. Depth distribution of neuronal activity related to a visual reaction time task in the monkey prefrontal cortex. *J. Neurophysiol.* **61**, 435–446 (1989).
- Sawaguchi, T., Matsumura, M. & Kubota, K. Catecholaminergic effects on neuronal activity related to a delayed response task in monkey prefrontal cortex. *J. Neurophysiol.* **63**, 1385–1400 (1990).
- Arnsten, A. F., Wang, M. J. & Paspalas, C. D. Neuromodulation of thought: flexibilities and vulnerabilities in prefrontal cortical network synapses. *Neuron* **76**, 223–239 (2012).
- Markowitz, D. A., Curtis, C. E. & Pesaran, B. Multiple component networks support working memory in prefrontal cortex. *Proc. Natl Acad. Sci. USA* **112**, 11084–11089 (2015).
- Bastos, A. M., Loonis, R., Kornblith, S., Lundqvist, M. & Miller, E. K. Laminar recordings in frontal cortex suggest distinct layers for maintenance and control of working memory. *Proc. Natl Acad. Sci. USA* **115**, 1117–1122 (2018).
- Barbey, A. K., Koenigs, M. & Grafman, J. Dorsolateral prefrontal contributions to human working memory. *Cortex* **49**, 1195–1205 (2013).
- Mackey, W. E., Devinsky, O., Doyle, W. K., Meager, M. R. & Curtis, C. E. Human dorsolateral prefrontal cortex is not necessary for spatial working memory. *J. Neurosci.* **36**, 2847–2856 (2016).
- Postle, B. R. et al. Repetitive transcranial magnetic stimulation dissociates working memory manipulation from retention functions in the prefrontal, but not posterior parietal. *Cortex. J. Cogn. Neurosci.* **18**, 1712–1722 (2006).
- Garey, L. J. et al. Reduced dendritic spine density on cerebral cortical pyramidal neurons in schizophrenia. *J. Neurol., Neurosurg. amp; Psychiatry* **65**, 446–453 (1998).
- Glantz, L. A. & Lewis, D. A. Decreased dendritic spine density on prefrontal cortical pyramidal neurons in schizophrenia. *Arch. Gen. Psychiatry* **57**, 65–73 (2000).
- Cannon, T. D. et al. Dorsolateral prefrontal cortex activity during maintenance and manipulation of information in working memory in patients with schizophrenia. *Arch. Gen. Psychiatry* **62**, 1071–1080 (2005).
- Wang, M., Vijayraghavan, S. & Goldman-Rakic, P. S. Selective D2 receptor actions on the functional circuitry of working memory. *Science* **303**, 853–856 (2004).
- Opris, I., Hampson, R. E., Stanford, T. R., Gerhardt, G. A. & Deadwyler, S. A. Neural activity in frontal cortical cell layers: evidence for columnar sensorimotor processing. *J. Cogn. Neurosci.* **23**, 1507–1521 (2011).
- Polimeni, J. R., Fischl, B., Greve, D. N. & Wald, L. L. Laminar analysis of 7 T bold using an imposed spatial activation pattern in human V1. *Neuroimage* **52**, 1334–1346 (2010).
- Kok, P., Bains, L. J., van Mourik, T., Norris, D. G. & de Lange, F. P. Selective activation of the deep layers of the human primary visual cortex by top-down feedback. *Curr. Biol.* **26**, 371–376 (2016).
- Muckli, L. et al. Contextual feedback to superficial layers of V1. *Curr. Biol.* **25**, 2690–2695 (2015).
- De Martino, F. et al. Frequency preference and attention effects across cortical depths in the human primary auditory cortex. *Proc. Natl Acad. Sci. USA* **112**, 16036–16041 (2015).
- Huber, L. et al. High-resolution CBV-fMRI allows mapping of laminar activity and connectivity of cortical input and output in human M1. *Neuron* **96**, 1253–1263.e1257 (2017).
- Corbitt, P. T., Ulloa, A. & Horwitz, B. Simulating laminar neuroimaging data for a visual delayed match-to-sample task. *NeuroImage* **173**, 199–222 (2018).
- D'Esposito, M., Postle, B. R., Ballard, D. & Lease, J. Maintenance versus manipulation of information held in working memory: an event-related fmri study. *Brain Cogn.* **41**, 66–86 (1999).
- Lu, H., Golay, X., Pekar, J. J. & Van Zijl, P. C. Functional magnetic resonance imaging based on changes in vascular space occupancy. *Magn. Reson. Med.: Off. J. Int. Soc. Magn. Reson. Med.* **50**, 263–274 (2003).
- Poser, B. A., Koopmans, P. J., Witzel, T., Wald, L. L. & Barth, M. Three dimensional echo-planar imaging at 7 tesla. *Neuroimage* **51**, 261–266 (2010).
- Petrides, M. & Pandya, D. Dorsolateral prefrontal cortex: comparative cytoarchitectonic analysis in the human and the macaque brain and corticocortical connection patterns. *Eur. J. Neurosci.* **11**, 1011–1036 (1999).
- Melchitzky, D. S., Sesack, S. R., Pucak, M. L. & Lewis, D. A. Synaptic targets of pyramidal neurons providing intrinsic horizontal connections in monkey prefrontal cortex. *J. Comp. Neurol.* **390**, 211–224 (1998).
- Medalla, M. & Barbas, H. Diversity of laminar connections linking periaruate and lateral intraparietal areas depends on cortical structure. *Eur. J. Neurosci.* **23**, 161–179 (2006).
- Wang, X.-J. Synaptic basis of cortical persistent activity: the importance of NMDA receptors to working memory. *J. Neurosci.* **19**, 9587–9603 (1999).
- Wang, M. et al. NMDA receptors subserve persistent neuronal firing during working memory in dorsolateral prefrontal cortex. *Neuron* **77**, 736–749 (2013).
- Bunge, S. A., Hazeltine, E., Scanlon, M. D., Rosen, A. C. & Gabrieli, J. Dissociable contributions of prefrontal and parietal cortices to response selection. *Neuroimage* **17**, 1562–1571 (2002).
- Jiang, Y. & Kanwisher, N. Common neural substrates for response selection across modalities and mapping paradigms. *J. Cogn. Neurosci.* **15**, 1080–1094 (2003).
- Curtis, C. E. & D'Esposito, M. Persistent activity in the prefrontal cortex during working memory. *Trends Cogn. Sci.* **7**, 415–423 (2003).
- Hadland, K. A., Rushworth, M. F. S., Passingham, R. E., Jahanshahi, M. & Rothwell, J. C. Interference with performance of a response selection task that has no working memory component: an RTMS comparison of the dorsolateral prefrontal and medial frontal cortex. *J. Cogn. Neurosci.* **13**, 1097–1108 (2001).
- Schumacher, E. H. & D'Esposito, M. Neural implementation of response selection in humans as revealed by localized effects of stimulus–response compatibility on brain activation. *Hum. Brain Mapp.* **17**, 193–201 (2002).
- Takada, M. et al. Organization of prefrontal outflow toward frontal motor-related areas in macaque monkeys. *Eur. J. Neurosci.* **19**, 3328–3342 (2004).
- Tomio, A., Kyoko, W. & Kisou, K. Connections of area 8 with area 6 in the brain of the macaque monkey. *J. Comp. Neurol.* **277**, 21–40 (1988).
- Arikuni, T. & Kubota, K. The organization of prefrontocaudate projections and their laminar origin in the macaque monkey: a retrograde study using Hrp-Gel. *J. Comp. Neurol.* **244**, 492–510 (1986).
- Yeterian, E. & Pandya, D. Laminar origin of striatal and thalamic projections of the prefrontal cortex in rhesus monkeys. *Exp. Brain Res.* **99**, 383–398 (1994).
- Perlstein, W. M., Carter, C. S., Noll, D. C. & Cohen, J. D. Relation of prefrontal cortex dysfunction to working memory and symptoms in schizophrenia. *Am. J. Psychiatry* **158**, 1105–1113 (2001).
- Kay, K. et al. A critical assessment of data quality and venous effects in ultra-high-resolution fMRI. *Neuroimage* **189**, 847–869 (2019).
- Goense, J., Merkle, H. & Logothetis, N. K. High-resolution fMRI reveals laminar differences in neurovascular coupling between positive and negative bold responses. *Neuron* **76**, 629–639 (2012).
- Kim, T. & Kim, S.-G. Cortical layer-dependent arterial blood volume changes: improved spatial specificity relative to bold fmri. *Neuroimage* **49**, 1340–1349 (2010).
- Yacoub, E., Ugurbil, K. & Harel, N. The spatial dependence of the poststimulus undershoot as revealed by high-resolution BOLD- and CBV-weighted fMRI. *J. Cereb. Blood Flow. Metab.* **26**, 634–644 (2006).
- Petridou, N. & Siero, J. C. Laminar fMRI: what can the time domain tell us? *NeuroImage* **197**, 761–771 (2017).
- Stephan, K. E. et al. Laminar fMRI and computational theories of brain function. *Neuroimage* **197**, 699–706 (2017).
- Lawrence, S. J. D., Formisano, E., Muckli, L. & de Lange, F. P. Laminar fMRI: applications for cognitive neuroscience. *Neuroimage* **197**, 785–791 (2019).

Acknowledgements

We thank A. Arnsten for guidance on experimental design and interpretation. We thank B. Poser and D. Ivanov for the 3D-EPI readout that is used in the VASO sequence here. We thank A.H. Hall and K. Chung for administrative support of human volunteer scanning. We thank S. Kashyap for helpful tips on adjusting manual initial registration used to generate Supplementary Fig. 2. We thank S. Marrett and D. Handwerker for technical advice and support. We thank A. Thomas and T. Riddle for support with data formatting, organization and sharing. Portions of this study used the high-performance computational capabilities of the Biowulf Linux cluster at the National Institutes of Health (biowulf.nih.gov). The research was funded by the National Institute of Mental Health Intramural Research Program (no. ZIAMH002783) to P.A.B., which also funded

E.S.F., L.H., D.C.J. and P.J.M. During the latest periods of data analysis, L.H. was funded from the NWO VENI project 016.Veni.198.032.

Author contributions

E.S.F. conceptualized the study, designed the task paradigm, collected the data, analyzed the data, generated visualizations and wrote the original manuscript. L.H. conceptualized the study, contributed to the task paradigm design, designed and optimized the data acquisition and analysis methodology, collected the data, analyzed the data, generated visualizations and wrote portions of the original manuscript. D.C.J. contributed to the task paradigm design, generated visualizations and provided comments on the manuscript. P.J.M. analyzed the data, generated visualizations and provided comments on the manuscript. P.A.B. supervised study conceptualization, design and interpretation, and provided comments on the manuscript.

Competing interests

The authors declare no competing interests.

Additional information

Supplementary information is available for this paper at <https://doi.org/10.1038/s41593-019-0487-z>.

Reprints and permissions information is available at www.nature.com/reprints.

Correspondence and requests for materials should be addressed to E.S.F.

Publisher's note Springer Nature remains neutral with regard to jurisdictional claims in published maps and institutional affiliations.

© The Author(s), under exclusive licence to Springer Nature America, Inc. 2019

Methods

Refer to the Nature Research Reporting Summary to access a subset of this information in a standardized format.

Subjects. Seventeen healthy volunteers participated after granting informed consent under an NIH Combined Neuroscience Institutional Review Board-approved protocol (93-M-0170, ClinicalTrials.gov identifier: NCT00001360) in accordance with the Belmont Report and US federal regulations that protect human subjects. Data from two subjects were excluded due to technical difficulties or experimenter error: in one subject, no clear activation was visible within the field of view (meaning the region of interest was likely outside the field of view), and in the second subject, an incorrect version of the task was used, resulting in altered event timings that made this subject's data incompatible with the rest of the data set. Of the remaining 15 subjects (age 20–47 years at the time of the experiment) whose data entered into the analyses presented here, eight were men and seven were nonpregnant women.

The functional data presented here come from a total 40 h of scan time collected in 20 2-h scan sessions. Two different functional acquisition protocols were used over the course of the study: an 'axial [readout] protocol' ($n = 15$ sessions) and a 'sagittal [readout] protocol' ($n = 5$ sessions); these are described further in their respectively titled sections below. Of the 15 unique subjects, $n = 8$ were scanned only once using the axial protocol; $n = 3$ were scanned once using the axial protocol and once using the sagittal protocol; $n = 2$ were scanned only once using the sagittal protocol and $n = 2$ were scanned twice on the axial protocol. Some overlap of subjects was by design, allowing us to assess test–retest reliability of our ROI location (see Supplementary Fig. 2). No statistical methods were used to pre-determine sample sizes, but our sample size is consistent with or larger than those reported in previous layer fMRI studies^{19–22,43,44}.

All fifteen subjects were invited for a separate scan session to obtain high-resolution reference anatomical T_1 -weighted data with a magnetization prepared-rapid gradient echo (MPRAGE)-based sequence. Five additional 2-h scan sessions were used as pilot experiments to optimize the task design and investigate motion limitations and sequence artifacts; data from these sessions are not shown.

Task paradigm. The task was created with PsychoPy2 software⁴⁹. For the axial readout protocol (repetition time (TR) = 2 s, described below), each trial consisted of the following periods (example, duration): letter string presentation (BDCAE, 2.5 s), fixation cross (+, 1.5 s), instruction cue (ALPHABETIZE or REMEMBER, 1 s), delay period with fixation cross (+, 9 s), probe (D? or *, 2 s), intertrial interval with fixation cross (+, 16 s). Subjects could register a response at any time after the appearance of the probe and before the start of the next trial (that is, anytime during the intertrial interval). Each trial thus lasted 32 s, and each run consisted of 20 trials plus brief (8 s) additional fixations at the beginning and end of the run, for a total of 10:56 min: per run. Runs alternated between two contrast types: (1) manipulation versus maintenance (consisting of a mix of ALPHABETIZE and REMEMBER trials, all requiring action) and (2) action versus nonaction (consisting of a mix of action and nonaction trials, all ALPHABETIZE). Within each run, the 10 trials of each type were presented in a fixed pseudorandom order that was the same for all runs, to facilitate averaging.

For the higher-resolution sagittal readout protocol (described below), all runs were of the first contrast type (manipulation versus maintenance), and trial-period timings were adjusted to match the longer TR of 2.5 s by scaling the duration of each period by a multiplier of 1.25. Each trial thus lasted 40 s and the duration of these runs was 13:40 min:s. All other parameters, including the pseudorandom order, were kept the same as above.

Before the start of the experimental runs, we ran a 6-min functional localizer that was conducted at standard resolution and analyzed in real time, allowing us to functionally define a region of interest within left dlPFC in each individual subject while the subject was in the scanner. This localizer consisted entirely of ALPHABETIZE trials and slightly altered timing. The length of all trial periods was as described above except the intertrial interval, which was shortened to 5 s to create a 10-s on, 10-s off paradigm. Delay-related activity (including cue plus delay-related fixation) was considered signal, whereas all other trial periods were treated as baseline. The location of peak activity from the real-time general linear model analysis was used to position the coverage of the subsequent submillimeter experiments.

Randomization and blinding. There were no experimental groups in this study; therefore, no randomization of subjects was necessary. As stated in the 'Task Paradigm' section above, within each run, the 20 trials (10 of each type) were presented in a fixed pseudorandom order that was the same for all subjects and all runs. This was done to facilitate averaging within subjects and to ensure a relatively even distribution of each trial type across the beginning, middle and end of runs (to mitigate concerns about signal drift that might differentially affect one trial type or the other).

Data collection and analysis were not performed blind to the conditions of the experiments. Subjects were not told the purpose of the study or specific hypotheses concerning differences between trial types and within-trial periods ahead of time but were debriefed following data collection upon request.

Experimental setup. All imaging was performed on a MAGNETOM 7-T scanner (Siemens Healthineers) with a single-channel-transmit/32-channel-receive head coil (Nova Medical). Imaging sessions did not exceed 120 min. Imaging slice position and slice angle were adjusted individually for every subject on the basis of the functional localizer described above.

A third-order B_0 -shim was done with three iterations using vendor-provided tools. The shim volume covered the entire imaging field of view (FOV) and was extended down to the circle of Willis to obtain sufficient B_0 homogeneity to exceed the adiabaticity threshold of the inversion pulse.

Following the functional localizer, for the axial protocol, run type alternated between the first contrast (alphabetize/remember) and the second contrast (action/nonaction). All subjects completed at least five runs (three of the alphabetize/remember contrast and two of the action/nonaction) per imaging session. Therefore there were 30 'alphabetize', 30 'remember', 20 'action' and 20 'nonaction' trials per subject per session. (Note that 'alphabetize' and 'action' trials are technically identical, although data were not pooled between these two conditions for analysis purposes given that they were acquired in different runs.) When time allowed (for $n = 6$ subject-sessions), a sixth run was acquired (action/nonaction contrast); these sessions thus comprised 30 of each trial type.

For the sagittal protocol, all runs were of the first contrast type (alphabetize/remember), and also consisted of 10 trials of each type (20 total), but note each trial was scaled to be longer in duration to match the TR of this protocol. Most subjects scanned with this protocol ($n = 3$) completed four total runs or 80 total trials (40 'alphabetize' and 40 'remember'). One subject completed three total runs (60 total trials/30 of each type) and one subject completed five runs (100 total trials/50 of each type).

Axial readout protocol. The protocol parameters were as follows: readout type, 3D-EPI with one segment per k -space plane²⁶; in-plane resolution, 0.91×0.91 mm²; slice thickness, 1.1 mm; fast low angle shot (FLASH) generalized autocalibrating partially parallel acquisitions (GRAPPA) 3; partial Fourier in the first phase encoding direction, 6/8; no partial Fourier in the second phase encoding direction; $TR_{VASO} = 2,000$ ms; $TR_{VASO+BOLD} = 4,000$ ms; FOV read and phase = 150 mm; matrix size = 162; echo time (TE) = 20 ms; read bandwidth = 1,144 Hz per pixel; phase echo spacing = 0.98. Assuming a gray-matter (GM) $T_2^* = 28$ ms, the expected T_2^* blurring for EPI-readout results in a signal leakage of 12% from one voxel into the neighboring voxels along the first phase-encoding direction. A more detailed list of scan parameters used can be found on GitHub: https://github.com/layerfMRI/Sequence_Github/blob/master/DLPFC_Emily/Emily_Intermediate_protocol.pdf.

Sagittal readout protocol. The protocol parameters were as follows: readout type, 3D-EPI with one segment per k -space plane²⁶; in-plane resolution, 0.75×0.75 mm²; slice thickness, 0.99 mm; FLASH GRAPPA 3; partial Fourier in the first phase encoding direction, 6/8; no partial Fourier in the second phase encoding direction; $TR_{VASO} = 2,500$ ms; $TR_{VASO+BOLD} = 5,000$ ms; FOV read = 130 mm; FOV phase, 98.8%; matrix size = 172; TE = 27 ms; read bandwidth = 908 Hz per pixel; phase echo spacing = 1.23 (limited by peripheral nerve stimulation thresholds). Assuming a GM $T_2^* = 28$ ms, the expected T_2^* blurring for EPI-readout results in a signal leakage of 14% from one voxel into the neighboring voxels along the first phase-encoding direction. A more detailed list of scan parameters used can be found on GitHub: https://github.com/layerfMRI/Sequence_Github/blob/master/DLPFC_Emily/DLPFC_high_res_076_076_1.pdf.

VASO-specific protocol parameters. Both readout protocols were acquired with the same VASO preparation module. The protocol parameters were thus: inversion pulse type, time resampled frequency offset corrected inversion (TR-FOCI) pulse with a bandwidth of 6.4 kHz, $\mu = 7$; pulse duration, 10 ms, nonselective. The phase skip of the adiabatic inversion pulse was adjusted to 30° to achieve an inversion efficiency of 80%, shorter than the arterial arrival time in the dlPFC⁵⁰. The inversion time was adjusted to match the blood-nulling time of 1,100 ms as done in previous studies²². To account for the T_1 -decay during the 3D-EPI readout and potential related blurring along the segment direction, a variable flip angle was chosen. The flip angle of the first segment was adjusted to be 22°. The subsequent flip angles were exponentially increasing, until last k -space segment was excited with a desired flip angle of 90°.

Image reconstruction. Image reconstruction was done in the vendor-provided platform, as done previously²². GRAPPA 3 kernel fitting was done on FLASH ACS data with a 3×4 kernel, 48 reference lines and regularization parameter $\chi = 0.001$. Radio frequency (RF) channels were combined with the sum-of-squares. To minimize resolution losses in the phase-encoding direction due to T_2^* -decay partial, Fourier reconstruction was done with POCS using eight iterations.

Anatomical reference data. In separate scan sessions, 0.7-mm resolution T_1 -maps were collected covering the entire brain with an MP2RAGE (magnetization prepared 2 rapid acquisition gradient echoes) sequence⁵¹ for every subject. These data were not used in the functional pipelines to analyze the layer-dependent activity changes. Instead, these images were used to investigate the reproducibility

of location of activity across sessions (Supplementary Fig. 2) and across subjects (Fig. 1c).

In four of the subjects that were invited for more than two 2-h sessions, slab-selective isotropic 0.5-mm and 0.4-mm resolution anatomical data were collected with MP2RAGE and multi-echo FLASH, respectively. Those anatomical data were not used in the pipeline for generating cortical profiles. They were used to validate the approximate position of the cytoarchitecturally defined cortical layers of individual subjects with respect to the 20 reconstructed cortical depths in which the functional data are processed (Supplementary Fig. 4).

Functional image preprocessing. This section describes processing steps that were common to both the axial and sagittal protocols. For a schematic overview of the analysis pipeline, see Supplementary Fig. 1.

First, DICOM (Digital Imaging and Communications in Medicine) images were converted to NIFTI (Neuroimaging Informatics Technology Initiative) format with the ISISCONV converter (Supplementary Fig. 1a). Motion correction was performed with SPM software (Statistical Parametric Mapping; SPM12)⁵² and was done separately for nulled and not-nulled frames (Supplementary Fig. 1b). A fourth-order spline function was used for spatial interpolation. Motion correction and registration across runs was done simultaneously. This minimized the effect of spatial resolution loss to one single resampling step⁵³. Motion traces of nulled and not-nulled images were visually inspected to ensure good overlap for the two contrasts (Supplementary Fig. 1b).

Following these steps, frames were sorted into their respective contrast: not-nulled (BOLD) or nulled (VASO; Supplementary Fig. 1c). Note that BOLD and VASO contrasts are kept separate from this point forward, and all analyses below were performed for each contrast individually.

Next, runs of the same contrast type were averaged (Supplementary Fig. 1d), and within these average runs, trials of the same type were averaged (Supplementary Fig. 1e). Because all runs have the same trial order, and all trials have the same epoch structure and timing, runs and trials can be averaged without deconvolving the hemodynamic response. This is an important feature of our experimental design, because hemodynamic responses differ across cortical depths⁴⁶. Following trial averaging, VASO data were BOLD corrected with the dynamic division method (Supplementary Fig. 1e). Thus, for each contrast (BOLD and VASO), for the axial protocol, each subject had four average trials: alphabetize, remember, action and nonaction. For the sagittal protocol, each subject had two average trials: alphabetize and remember.

In a parallel analysis, a region of interest (ROI) in the left dlPFC was defined for each subject (Supplementary Fig. 1f). The approximate location of the ROI was taken from the 6-min functional localizer (Supplementary Fig. 1f, left) following general linear model analysis with FSL FEAT (v.5.98)⁵⁴. For the complete FEAT design protocol, please see (https://github.com/layerfMRI/repository/tree/master/DLPFC_Emily/Featdesign). The ROI was manually selected and drawn for every individual subject (see Supplementary Fig. 3 for drawn ROIs in every subject). Rather than only acquire an additional T_1 -weighted image for anatomical reference, we used the functional EPI data itself to estimate the T_1 contrast and used this for manual delineation of two layers within this ROI, one superficial and one deep (Supplementary Fig. 1f, right). The advantage of this approach is that it avoids the distortion correction and resampling steps necessary for registering EPI images to a separately acquired T_1 image, preserving spatial specificity. See sections below for additional information about this layer-drawing procedure for both the axial and sagittal protocols.

Layering and time course extraction for axial protocol. This section describes the steps applied to data acquired with the axial protocol and shown in Figs. 2 and 3. The manual drawing of the layer masks was done according to the following guidelines: a) layers were drawn as a connected collection of voxels without holes; b) the superficial layer was positioned such that there was no partial voluming with the cerebrospinal fluid (CSF); c) the deeper layer was positioned such that there was no partial voluming with white matter (WhM); d) the superficial and deeper layers were eroded until there was no residual overlap of superficial and deeper layers; e) the thickness of the superficial and deeper layers were kept similar along the cortical ribbon; f) the thickness of the superficial and deeper layers was chosen such that they filled as much of the cortex as possible without violating the guidelines above; and g) for consistency, the same person drew the layers for all subjects. The results of all drawings are shown in Supplementary Fig. 3.

Next, at each time point, signal was averaged across all voxels within each layer to derive one average time course per layer in each of the four trial types. Thus, each subject had eight time courses: one per layer (superficial, deeper) per trial type (alphabetize, remember, action, nonaction; Supplementary Fig. 1g).

Before pooling data across subjects, BOLD time courses were normalized within subjects by the following steps. First, a per-layer (y) mean baseline BOLD signal (\bar{b}_y) was calculated by averaging signal during baseline time points across all four trial types (where 'baseline time points' include the first time point, which is before the appearance of the stimulus, and the penultimate and ultimate time points, which are 18 and 22 s after the appearance of the probe, the point at which signal is expected to have returned to at or near baseline). Next, the BOLD

signal s for layer y at time point t was transformed to s' as follows, to yield values interpretable as percentage signal change:

$$S'_{y,t} = \frac{S_{y,t}}{\bar{b}_y} \times 100 - 100$$

Note that unlike BOLD, VASO is a quantitative measure that is proportional to a physical unit (ml per 100-ml tissue volume), meaning units can be directly interpreted and it is not necessary to convert to percentage signal change. VASO data were instead transformed as follows. First, to facilitate interpretation, each subject's VASO signal v at each time point t was transformed from a negative to a positive contrast as thus:

$$V_t = V_t \times -100$$

Following this, VASO signals were normalized within subjects by calculating a per-layer mean baseline VASO signal (\bar{v}_y) by averaging signal during baseline time points (same time points as for BOLD above) across all four trial types. This mean baseline signal was subtracted from each time point as follows:

$$v'_{y,t} = v_{y,t} - \bar{v}_y$$

All the subsequent statistical contrasts were performed directly on these normalized signal time courses. We refrained from using deconvolution or inferential statistical models (for example, general linear models) to measure activation, to avoid biases of variable noise magnitudes and hemodynamical response functions across cortical depths.

For purposes of the two-way, repeated-measures ANOVA depicted in Figs. 2b, 3b and Supplementary Fig. 5b, the representative delay signal was the average of VASO measurements acquired at time points 4, 5 and 6 (corresponding to 12, 16 and 20 s in trial time), and the representative response signal was the average of VASO measurements acquired at time points 7 and 8 (corresponding to 24 and 28 s in trial time). Although the repeated-measures ANOVA test is robust against violations of the assumption of normality, it does assume sphericity, which refers to the condition where the variances of the differences between all possible pairs of within-subject conditions (that is, levels of the independent variable) are equal. Because there is currently no clear way to test for sphericity for the interaction term of a two-way repeated measures ANOVA (our main term of interest), here, we report the Greenhouse-Geisser-corrected P value⁵⁵ for all tests, which is a conservative form of correction that is recommended when nothing is known about the sphericity of the data⁵⁶.

Layering for sagittal protocol. This section describes image processing for the single-subject, layer-dependent activity profiles acquired with the sagittal protocol and shown in Fig. 4. Cortical depths were estimated directly in EPI space without alignment to so-called anatomical space. This procedure minimizes the risk of resolution loss due to multiple spatial resampling steps and avoids any potential errors in distortion correction and registration. An anatomical reference contrast was calculated from the functional data by calculating the inverse signal variability across nulled and not-nulled images, divided by the mean signal. This measure is called here T_1 -EPI and provides a good contrast between white matter (WhM), gray matter (GM) and cerebro-spinal fluid (CSF; see background images in Fig. 4, Supplementary Figs. 1 and 3). Borderlines between GM/WhM and GM/CSF are manually drawn based on this contrast. The manual drawing was done as described in previous publications^{22,57–59} according to the following guidelines: (a) borderlines were drawn as continuous lines without holes; (b) the lines are drawn such that their curvature radius was kept smaller than the cortical thickness; (c) the position of the GM/CSF border was drawn through voxels that were just above the GM, such that there was no GM partial voluming; (d) the position of the GM/WhM border was drawn through voxels that were just below the GM, such that there was no GM partial voluming—this means that the position of the voxels that are half filled with GM are in the respective upper-most and lower-most extracted layers; (e) for consistency, the same person drew the layers for all subjects.

Manually drawn border lines are shown for all subjects in Fig. 4c (bright yellow for GM/CSF and bright blue for GM/WhM). Twenty-one layers were calculated between these borderlines with the LAYNII program LN_GROW_LAYERS (<https://github.com/layerfMRI/LAYNII>). To minimize partial volume effects and allow the calculation of smooth layers, the layering calculation was applied on a four-fold finer grid than the native functional resolution. This means that the number of layers is higher than the number of independent voxels sampled across the cortical depth. The number of layers should not be confused with the effective resolution across cortical depths. Given the cortical thickness of 3.5–4 mm in dlPFC^{60,61}, the resolution of 0.76 mm in-plane and 0.99 mm slice thickness is sufficient to sample 3–6 independent voxels across cortical depth. This amount is enough to estimate activity in superficial and deeper layers (red-yellow compared to blue-turquoise in Fig. 4c) with Nyquist sampling. The number 21 was chosen based on previous experience in finding a compromise between data size and smoothness (see Supplementary Fig. 6 in ref. ⁵⁸ as well as refs. ^{22,57}).

For best visibility, functional signals were smoothed along the tangential direction of the cortex (that is, within 'layers') with a Gaussian kernel of 0.76 mm.

To maintain the spatial specificity across layers, no smoothing was applied across cortical depths. This kind of layer smoothing can improve the detectability of fMRI signal changes without unwanted leakage of physiological noise above the cortical surface^{23,58,62}. The application of such layer smoothing is based on the assumption that neighboring columnar structures are similarly engaged during the task. See Supplementary Fig. 8 for a discussion of variance in the functional response across columns. Note that the batch of cortex investigated here is highly folded with respect to the external magnetic field. This means that the BOLD signal change can be substantially variable dependent on the columnar position along the sulcus^{63,64}.

Interpreting cortical depth-dependent results with respect to cytoarchitectonic layers.

To interpret the fMRI results according to known input–output characteristics of different cortical layer groups II/III and V/VI, it is helpful to approximate the location of functional activity with respect to underlying layers as defined cytoarchitectonically. To confirm the approximate borders and the different layers within these borders, we followed the approach outlined in earlier work⁶⁵. This is a three-step approach: First, we extracted layer signatures in high-resolution multimodal post-mortem histology data of an individual cadaver brain sample from the Ding Atlas⁶⁶. Second, we identified the MR-sensitive features and landmarks⁶⁷ in anatomical MRI scans from a subject from our study and estimated their relative position across the cortical thickness. Third, we used these features as markers of the cytoarchitectonic layers in the functional data from the same participant to confirm the relative depth position of the functional responses. With this procedure, we can attempt to interpret the layer origin of the functional signal solely based on the relative depth of the cortical thickness. The results of this procedure are shown in Supplementary Fig. 4.

Note that this approach of comparing fMRI data with histology data is not conducted as part of the fMRI analysis pipeline. The time courses and layer profiles shown here are solely extracted based on relative distance to the GM/CSF and GM/WhM borderlines. The comparison of the relative cortical depth in fMRI data and histology data is based on the assumption that the relative position of the cytoarchitectonic layers and their relative thicknesses is the same across subjects (see insets in Fig. 4c).

Spatial alignment across sessions (within-subject). Note that all layer data are taken from individual sessions and are thus not susceptible to potential registration errors across days. However, it is important to ensure that the location of activity is generally consistent with a single subject across days and imaging sessions.

To investigate this consistency in the two subjects on whom we collected test–retest data (that is, two imaging sessions separately by several days), each session's layer masks and the corresponding activation maps were transformed into subject-specific anatomical reference spaces. Registration was done with SyN in ANTs (Advanced Normalization Tools⁶⁸) with a spline interpolation. Since the imaging coverage of the functional data is significantly smaller than the whole brain, it was necessary to provide a manual starting point for the ANTs registration to converge on reasonable registration quality. The initial manual registration was done in ITK-SNAP. The registration from EPI-space to the subject-specific anatomical space was done by means of the similar T_1 contrast of T_1 -EPI and the MP2RAGE UNI-DEN image. The same spatial operation was applied to the layer masks and the functional activation maps. The resulting activation patterns were compared across days in the anatomical space of individual subjects (Supplementary Fig. 2). Note that the registration quality here did not need to achieve accuracy levels at the submillimeter layer scale. Instead, the goal of this analysis was to demonstrate that the process of ROI selection (several millimeters large) was reproducible.

Spatial alignment across subjects (mean ROI location). To verify placement of the ROI taken from the functional localizer, and to create the group-level image shown in Fig. 1c, we processed data from the localizer run in AFNI⁶⁹, using the standard 'super-script' `afni_proc.py`. Each subject's high-resolution (T_1 -MPRAGE) whole-brain anatomical data were registered to the MNI 152 template with a combined affine and nonlinear warp. To minimize interpolation, this transformation was concatenated with both the affine transform used to register the echo-planar images to the individual-subject anatomical data, as well as the rigid (six degrees of freedom) warp to account for subject motion. Data were then smoothed with a 4-mm (2 voxels) Gaussian kernel, scaled to percentage signal change and submitted to a multiple regression. The standard boxcar block design was convolved with the hemodynamic response function along with six motion parameters (three translation, three rotation). Group analyses were conducted in 3dttest++, which yielded a cluster in left dlPFC with a whole-brain map at voxelwise $P < 0.01$. This cluster represents the approximate location where the higher-resolution layer slices were prescribed in the subsequent experimental runs,

and is included here for convenience as a post hoc visualization of the macroscale location of our ROI.

Reporting Summary. Further information on research design is available in the Nature Research Reporting Summary linked to this article.

Data availability

Data are available via OpenNeuro at the following link: <https://doi.org/10.18112/openneuro.ds002076.v1.0.1>

Code availability

All code is available in the following GitHub repository: https://github.com/layerfMRI/repository/tree/master/DLPFC_Emily

References

- Peirce, J. W. Psychopy—psychophysics software in python. *J. Neurosci. Methods* **162**, 8–13 (2007).
- Mildner, T. et al. Mapping of arterial transit time by intravascular signal selection. *NMR Biomed.* **27**, 594–609 (2014).
- Marques, J. P. et al. MP2RAGE, a self bias-field corrected sequence for improved segmentation and T1-mapping at high field. *Neuroimage* **49**, 1271–1281 (2010).
- Friston, K. J. et al. Statistical parametric maps in functional imaging: a general linear approach. *Hum. Brain Mapp.* **2**, 189–210 (1994).
- Polimeni, J. R., Reznall, V., Zaretskaya, N. & Fischl, B. Analysis strategies for high-resolution UHF-fMRI data. *NeuroImage* **168**, 296–320 (2018).
- Worsley, K. Statistical analysis of activation images. *Funct. MRI: Introd. Methods* **14**, 251–270 (2001).
- Greenhouse, S. W. & Geisser, S. On methods in the analysis of profile data. *Psychometrika* **24**, 95–112 (1959).
- Girden, E. R. *Anova: Repeated Measures* (Sage, 1992).
- Huber, L., Uludağ, K. & Möller, H. E. Non-bold contrast for laminar fMRI in humans: CBF, CBV, and CMRO2. *Neuroimage* **197**, 742–760 (2017).
- Huber, L. et al. Ultra-high resolution blood volume fMRI and bold fMRI in humans at 9.4 T: capabilities and challenges. *Neuroimage* **178**, 769–779 (2018).
- Huber, L. et al. Techniques for blood volume fMRI with VASO: from low-resolution mapping towards sub-millimeter layer-dependent applications. *Neuroimage* **164**, 131–143 (2018).
- Fischl, B. & Dale, A. M. Measuring the thickness of the human cerebral cortex from magnetic resonance images. *Proc. Natl Acad. Sci.* **97**, 11050–11055 (2000).
- Williams, S. M. & Goldman-Rakic, P. S. Characterization of the dopaminergic innervation of the primate frontal cortex using a dopamine-specific antibody. *Cereb. cortex* **3**, 199–222 (1993).
- Blazejewska, A. I., Fischl, B., Wald, L. L. & Polimeni, J. R. Intracortical smoothing of small-voxel fMRI data can provide increased detection power without spatial resolution losses compared to conventional large-voxel fMRI data. *Neuroimage* **189**, 601–614 (2019).
- Gagnon, L. et al. Quantifying the microvascular origin of bold-fMRI from first principles with two-photon microscopy and an oxygen-sensitive nanoprobe. *J. Neurosci.* **35**, 3663–3675 (2015).
- Fracasso, A., Luijten, P. R., Dumoulin, S. O. & Petridou, N. Laminar imaging of positive and negative BOLD in human visual cortex at 7t. *Neuroimage* **164**, 100–111 (2018).
- Geyer, S., Weiss, M., Reimann, K., Lohmann, G. & Turner, R. Microstructural parcellation of the human cerebral cortex—from Brodmann's post-mortem map to in vivo mapping with high-field magnetic resonance imaging. *Front. Hum. Neurosci.* **5**, 19 (2011).
- Ding, S.-L. et al. Comprehensive cellular-resolution atlas of the adult human brain. *J. Comp. Neurol.* **524**, 3127–3481 (2016).
- Stüber, C. et al. Myelin and iron concentration in the human brain: a quantitative study of MRI contrast. *Neuroimage* **93**, 95–106 (2014).
- Avants, B. B., Epstein, C. L., Grossman, M. & Gee, J. C. Symmetric diffeomorphic image registration with cross-correlation: evaluating automated labeling of elderly and neurodegenerative brain. *Med. Image Anal.* **12**, 26–41 (2008).
- Cox, R. W. AFNI: software for analysis and visualization of functional magnetic resonance neuroimages. *Comput. Biomed. Res.* **29**, 162–173 (1996).

Reporting Summary

Nature Research wishes to improve the reproducibility of the work that we publish. This form provides structure for consistency and transparency in reporting. For further information on Nature Research policies, see [Authors & Referees](#) and the [Editorial Policy Checklist](#).

Statistics

For all statistical analyses, confirm that the following items are present in the figure legend, table legend, main text, or Methods section.

n/a Confirmed

- The exact sample size (n) for each experimental group/condition, given as a discrete number and unit of measurement
- A statement on whether measurements were taken from distinct samples or whether the same sample was measured repeatedly
- The statistical test(s) used AND whether they are one- or two-sided
Only common tests should be described solely by name; describe more complex techniques in the Methods section.
- A description of all covariates tested
- A description of any assumptions or corrections, such as tests of normality and adjustment for multiple comparisons
- A full description of the statistical parameters including central tendency (e.g. means) or other basic estimates (e.g. regression coefficient) AND variation (e.g. standard deviation) or associated estimates of uncertainty (e.g. confidence intervals)
- For null hypothesis testing, the test statistic (e.g. F , t , r) with confidence intervals, effect sizes, degrees of freedom and P value noted
Give P values as exact values whenever suitable.
- For Bayesian analysis, information on the choice of priors and Markov chain Monte Carlo settings
- For hierarchical and complex designs, identification of the appropriate level for tests and full reporting of outcomes
- Estimates of effect sizes (e.g. Cohen's d , Pearson's r), indicating how they were calculated

Our web collection on [statistics for biologists](#) contains articles on many of the points above.

Software and code

Policy information about [availability of computer code](#)

Data collection

A slice-selective slab-inversion (SS-SI) vascular space occupancy (VASO) pulse sequence (Huber et al., 2014; ref. 26) was implemented on a MAGNETOM 7T scanner (Siemens Healthineers, Erlangen, Germany) using the vendor-provided IDEA environment (VB17A-UHF). For RF transmission and reception, a single-channel-transmit/32-channel-receive head coil (Nova Medical, Wilmington, MA, USA) was used. The scanner was equipped with a SC72 body gradient coil (maximum effective gradient strength used here: 49 mT/m; maximum slew rate used: 199 T/m/s). A 3rd-order B0-shim was done with three iterations using vendor-provided tools. The shim volume covered the entire imaging field of view (FOV) and was extended down to the circle of Willis in order to obtain sufficient B0-homogeneity to exceed the adiabaticity threshold of the inversion pulse.

PsychoPy2 (version 1.85.6) was used to create and present the task stimuli.

Data analysis

The following openly available tools were used for various steps in the data analysis pipeline as described in Methods:
 FSL Software Library v5.0 FMRIB, Oxford (<https://fsl.fmrib.ox.ac.uk/fsl/fslwiki>)
 Statistical Parametric Mapping (SPM) v12 Wellcome Trust Centre for Neuroimaging, UCL (<http://www.fil.ion.ucl.ac.uk/spm/>)
 Advanced Normalization Tools (ANTs) version 2.2.0 (<http://stnava.github.io/ANTs/>)
 ITK-SNAP version 3.6.0 (<http://www.itksnap.org/pmwiki/pmwiki.php>)
 LAYNII version 1.0.0 (<https://github.com/layerfMRI/LAYNII>)
 AFNI version 19.1.01 (<https://afni.nimh.nih.gov>)

Custom data-analysis code written for this study is available at:
https://github.com/layerfMRI/repository/tree/master/DLPFC_Emily

For manuscripts utilizing custom algorithms or software that are central to the research but not yet described in published literature, software must be made available to editors/reviewers. We strongly encourage code deposition in a community repository (e.g. GitHub). See the Nature Research [guidelines for submitting code & software](#) for further information.

Data

Policy information about [availability of data](#)

All manuscripts must include a [data availability statement](#). This statement should provide the following information, where applicable:

- Accession codes, unique identifiers, or web links for publicly available datasets
- A list of figures that have associated raw data
- A description of any restrictions on data availability

All raw data are publicly available through OpenNeuro.org: <https://doi.org/10.18112/openneuro.ds002076.v1.0.1>

Field-specific reporting

Please select the one below that is the best fit for your research. If you are not sure, read the appropriate sections before making your selection.

Life sciences Behavioural & social sciences Ecological, evolutionary & environmental sciences

For a reference copy of the document with all sections, see [nature.com/documents/nr-reporting-summary-flat.pdf](https://www.nature.com/documents/nr-reporting-summary-flat.pdf)

Life sciences study design

All studies must disclose on these points even when the disclosure is negative.

| | |
|-----------------|--|
| Sample size | The functional data in this study are from 15 subjects scanned in a combined total of 20 functional imaging sessions. Due to the inter-subject anatomical variability in the submillimeter meso-scale, the scan slots were used to do multiple comprehensive experiments in the same subjects rather than short experiments in a larger cohorts. This is consistent with other recent layer fMRI studies (Muckli et al., Current Biology 2015 [4 subjects, with retest]; De Martino et al., PNAS 2015 [5 subjects, with retest]; Kok et al., Current Biology 2016 [11 subjects, no retest]; Huber et al., Neuron 2017 [11 subjects, some with retest]). |
| Data exclusions | Data from two additional subjects were excluded due to technical difficulties or experimenter error: in one subject, no clear activation was visible within the field of view (meaning the region of interest was likely outside the field of view), and in the second subject, an incorrect version of the task was used, resulting in altered event timings that made this subject's data incompatible with the rest of the dataset. |
| Replication | See Fig. S6 and S7 for average timecourses from single subjects showing that our main result of interest is visible in the vast majority of individual subjects (in addition to the group-level data shown in the main figures). Furthermore, we were able to observe depth-dependent activity maps in 5/5 subjects studied with the ultra-high-resolution protocol, which permits visualization of single-subject data directly on brain slices (see Fig. 4). Additionally, of the 13 unique subjects in the axial study, 2 were brought back for a retest session to confirm that the location of peak DLPFC activation is consistent across days (see Fig. S2). |
| Randomization | Randomization not applicable since there were no groups in this study. |
| Blinding | Blinding not applicable since there were no groups in this study. |

Reporting for specific materials, systems and methods

We require information from authors about some types of materials, experimental systems and methods used in many studies. Here, indicate whether each material, system or method listed is relevant to your study. If you are not sure if a list item applies to your research, read the appropriate section before selecting a response.

Materials & experimental systems

| n/a | Involved in the study |
|-------------------------------------|---|
| <input checked="" type="checkbox"/> | <input type="checkbox"/> Antibodies |
| <input checked="" type="checkbox"/> | <input type="checkbox"/> Eukaryotic cell lines |
| <input checked="" type="checkbox"/> | <input type="checkbox"/> Palaeontology |
| <input checked="" type="checkbox"/> | <input type="checkbox"/> Animals and other organisms |
| <input type="checkbox"/> | <input checked="" type="checkbox"/> Human research participants |
| <input checked="" type="checkbox"/> | <input type="checkbox"/> Clinical data |

Methods

| n/a | Involved in the study |
|-------------------------------------|--|
| <input checked="" type="checkbox"/> | <input type="checkbox"/> ChIP-seq |
| <input checked="" type="checkbox"/> | <input type="checkbox"/> Flow cytometry |
| <input type="checkbox"/> | <input checked="" type="checkbox"/> MRI-based neuroimaging |

Human research participants

Policy information about [studies involving human research participants](#)

Population characteristics Fifteen healthy volunteers (8 male, 7 non-pregnant female; age range 20-47 years) participated in this study. No genotyping was conducted.

Recruitment

Subjects were recruited via advertisements in and around the NIH and local Bethesda, Md. community. Due to the nature of the scanning environment at 7T, which features a narrower scanner bore and higher intensity of magnetic field than experiments at 3T, when possible, we gave preference to subjects who had participated in 7T studies in the past (or at least several 3T studies) and were known to tolerate the scanning environment well and have low head motion. This focus on particularly healthy and compliant subjects likely resulted in cleaner data relative to a true community sample.

Ethics oversight

The protocol (93-M-0170, ClinicalTrials.gov identifier: NCT00001360) was approved by the NIH Combined Neuroscience Institutional Review Board-approved protocol in accordance with the Belmont Report and US federal regulations that protect human subjects.

Note that full information on the approval of the study protocol must also be provided in the manuscript.

Magnetic resonance imaging

Experimental design

Design type

Task, event-related

Design specifications

For the axial readout protocol (TR = 2s), each trial consisted of the following epochs (example, duration): letter string presentation (BDCAE, 2.5 s), fixation cross (+, 1.5 s), instruction cue (ALPHABETIZE or REMEMBER, 1 s), delay period with fixation cross (+, 9 s), probe (D? or *?, 2 s), inter-trial interval with fixation cross (+, 16 s). Each trial thus lasted 32 s, and each run consisted of 20 trials plus brief (8 s) additional fixations at the beginning and end of the run, for a total of 10:56 min:sec per run. Runs alternated between two contrast types: (1) manipulation versus maintenance (consisting of a mix of ALPHABETIZE and REMEMBER trials, all requiring action), and (2) action versus non-action (consisting of a mix of action and non-action trials, all ALPHABETIZE). Within each run, the 10 trials of each type were presented in a pseudorandom order that was the same for all runs, to facilitate averaging. For the higher-resolution sagittal readout protocol (described below), trial epoch timings were adjusted to match the longer TR (2.5 s) by scaling the duration of each epoch by a multiplier of 1.25. Each trial thus lasted 40 s, and the duration of these runs was 13:40 min:sec. All sagittal-readout runs were of the first contrast type (manipulation versus maintenance). All other parameters, including the pseudorandom order, were kept the same as described for the axial readout protocol.

Behavioral performance measures

Button presses were recorded for accuracy and reaction time. Subjects performed well on the task (overall mean accuracy = 0.82, s.d. = 0.13, range = 0.59 – 0.97; note that chance is approximately 0.2), including both manipulation trials (mean (s.d.), range: 0.79 (0.13), 0.54 – 0.96) and maintenance trials (mean (s.d.), range: 0.88 (0.15), 0.53 – 1.0). Subjects were less accurate on manipulation compared to maintenance trials (paired t-test, $t_{14} = -3.28$, $p = 0.01$), which is expected given previous reports using this task. Overall mean reaction time (RT) was 2.37 s (s.d., range: 1.24, 1.05 – 5.17). Crucially, there was no difference between mean RT on manipulation versus maintenance trials (paired t-test, $t_{14} = 1.29$, $p = 0.22$).

Acquisition

Imaging type(s)

functional

Field strength

7T

Sequence & imaging parameters

Axial readout protocol

In-plane voxel resolution was 0.9 mm with a slice thickness of 1.1 mm. The protocol parameters were as follows: Readout type: 3D-EPI with one segment per k-space plane, in-plane resolution 0.91 x 0.91 mm², slice thickness 1.1 mm, FLASH GRAPPA 3, partial Fourier in the first phase encoding direction: 6/8, no partial Fourier in the second phase encoding direction, TR(VASO) = 2000 ms, TR(VASO+BOLD) = 4000 ms, FOV read and phase = 150 mm, matrix size = 162, TE = 20 ms, read bandwidth = 1144 Hz/Px, phase echo spacing = 0.98. Assuming gray-matter T2* = 28 ms, the expected T2* blurring for EPI-readout results in a signal leakage of 12% from one voxel into the neighboring voxels along the first phase-encoding direction. A more detailed list of scan parameters used can be found on GitHub: https://github.com/layerfMRI/Sequence_Github/blob/master/DLPFC_Emy/Emily_Intermediate_protocol.pdf.

Sagittal readout protocol

The protocol parameters are as follows: Readout type: 3D-EPI with one segment per k-space plane, in-plane resolution 0.75 x 0.75 mm², slice thickness 0.99 mm, FLASH GRAPPA 3, partial Fourier in the first phase encoding direction: 6/8, no partial Fourier in the second phase encoding direction, TR(VASO) = 2500 ms, TR(VASO+BOLD) = 5000 ms, FOV read = 130 mm, FOV phase 98.8%, matrix size = 172, TE = 27 ms, read bandwidth = 908 Hz/Px, phase echo spacing = 1.23 (limited by peripheral nerve stimulation thresholds). Assuming gray-matter T2* = 28 ms, the expected T2* blurring for EPI-readout results in a signal leakage of 14% from one voxel into the neighboring voxels along the first phase-encoding direction. A more detailed list of scan parameters used can be found on GitHub: https://github.com/layerfMRI/Sequence_Github/blob/master/DLPFC_Emy/DLPFC_high_res_076_0.76_1.pdf.

VASO-specific protocol parameters

Both readout protocols were acquired with the same VASO preparation module. The protocol parameters were: Inversion pulse type: TR-FOCI pulse with a bandwidth of 6.4 kHz, $\mu = 7$, pulse duration: 10 ms, non-selective. The phase skip of the adiabatic inversion pulse was adjusted to 30 deg to achieve an inversion efficiency of 80%, shorter than the arterial arrival time in the dIPFC (ref. 46). The inversion time was adjusted to match the blood-nulling time of 1100 ms as done in previous studies (ref. 19). To account for the T1-decay during the 3D-EPI readout and potential related blurring along the segment direction, a variable flip angle was chosen. The flip angle of the first segment was adjusted to be 22 deg. The subsequent flip angles were exponentially increasing, until last k-space segment was

excited with a desired flip angle of 90 deg.

Area of acquisition

The limitations on the parameter spaces of the high-resolution fMRI pulse sequences used in this study currently do not permit a whole-brain field of view. Therefore, data were acquired from a slab (positioned either axially or sagittally, depending on the readout protocol; see Methods) centered on a region of interest (ROI) in dorsolateral prefrontal cortex (dlPFC). Prefrontal cortex is large, and quite variable across individuals in terms of structure and functional anatomy. Unlike other cortical landmarks, such as the 'hand knob' of the primary motor cortex, functional subdivisions of dlPFC are difficult to pinpoint in individual participants using macroscale anatomical features. Therefore, regions of interest (ROIs) were selected for each participant on the basis of an online functional localizer conducted just prior to the experimental task runs. This initial 6-minute experiment was conducted at standard resolution and analyzed in real time, allowing us to functionally define a region of interest within dlPFC in each individual participant while the participant was in the scanner. The location of peak activity from the real-time analysis was used to position the coverage of the subsequent sub-millimeter experiments. Results showed good overlap between ROIs derived from independent experimental sessions (Fig. S2), indicating that the functional region in question can be reliably localized within participants.

Diffusion MRI

Used

Not used

Preprocessing

Preprocessing software

DICOM images were converted to NIFTI using the ISICONV converter. Motion correction was performed using SPM software (Statistical Parametric Mapping; SPM12; ref. 47) and was done separately for nulled and not-nulled frames (Fig. S1b). A 4th order spline function was used for spatial interpolation. Motion correction and registration across runs was done simultaneously. This minimized the effect of spatial resolution loss to one single resampling step (ref. 48). Motion traces of nulled and not-nulled were visually inspected to ensure good overlap for the two contrasts (Fig. S1b).

Normalization

Within-subject normalization:

Rather than acquire an additional T1-weighted image for anatomical reference, we used each subject's functional EPI data itself to estimate the T1 contrast, and used this derived T1 image for manual delineation of two layers within the dlPFC ROI, one superficial and one deep (Fig. S1f, S2a). The advantage of this approach is that it avoids the distortion correction and resampling steps necessary for registering EPI images to a separately acquired T1 image, preserving spatial specificity.

Across-subject normalization:

Individual-subject data were not normalized to a group-template space for the primary analyses presented in this study. Rather, average layer timecourses were extracted from each subject's dlPFC ROI (one superficial and one deep) and these timecourse data were then pooled across subjects and submitted to statistical hypothesis testing. Where possible, individual-subject data were also visualized on their own (e.g., Fig. 4). In a post-hoc analysis, to better specify our macroscale position within dlPFC, we estimated and visualized the average ROI location across participants (Fig. 1c). This analysis did require normalization to an MNI-template space. To this end, we processed data from the localizer run in AFNI, using the standard "super-script" afni_proc.py. Each subject's high-resolution (T1-MPRAGE) whole-brain anatomical data were registered to the MNI 152 template using a combined affine and nonlinear warp. To minimize interpolation, this transformation was concatenated with both the affine transform used to register the echo-planar images to the individual-subject anatomical data, as well as the rigid (6 degrees of freedom) warp to account for subject motion. Data were then smoothed using a 4mm (2 voxels) Gaussian kernel, scaled to percent signal change, and submitted to a multiple regression. The standard boxcar block design was convolved with the HRF along with six motion parameters (3 translation, 3 rotation). Group analyses were conducted in 3dttest++, which yielded a cluster in left dlPFC with a whole-brain map at voxelwise $p < 0.01$. This cluster represents the approximate location where the higher-resolution layer slices were prescribed in the subsequent experimental runs.

Normalization template

MNI152 template brain (where applicable; see answer above)

Noise and artifact removal

Data were motion corrected, but we did not regress any noise or artifact signals in the preprocessing pipeline.

Volume censoring

No volume censoring was conducted.

Statistical modeling & inference

Model type and settings

No voxelwise statistical inference was performed as part of this study (with the exception of the group-level analysis of functional localizer data, which was done for purposes of post-hoc ROI visualization [Fig. 1c] as described in the "Normalization" section above). Note that, again with the exception of the functional localizer data, we refrain from using statistical general linear model (GLM) deconvolution with predefined hemodynamic response functions (HRFs). Rather, we extract quantitative VASO signal differences that are obtained at the same latency within the respective trials of interest (e.g., delay-period signal in manipulation ['alphabetize'] trials versus delay-period signal in maintenance ['remember'] trials) and perform statistical inference on these values, as described below. A task design that allows us to avoid GLM deconvolution is a strength of this study, because results of depth-dependent GLMs can be hard to interpret for the following reasons: (1) HRFs are different across cortical depths; (2) the signal quality and stability are heterogeneous across cortical depths; and (3) the baseline blood volume distribution varies across the cortical depth.

For group-level analysis of the functional localizer data, we used a multiple regression model including a standard boxcar block design (10s on, 10s off) convolved with the HRF, along with six motion parameters (3 translation, 3 rotation). This analysis was conducted using AFNI's 3dttest++ program.

Effect(s) tested

To quantitatively compare activity within cortical depths, we performed a series of two-way, repeated-measures analyses of variance (ANOVAs) using representative signals from each trial type during each trial period. The representative delay signal was the average of VASO measurements acquired at timepoints 4, 5 and 6 (corresponding to 12, 16 and 20 sec in trial time), and the representative response signal was the average of VASO measurements acquired at timepoints 7 and 8 (corresponding to 24 and 28 sec in trial time). In each ANOVA, the two factors were trial type (either 'alphabetize' and 'remember', or 'action' and 'non-action') and trial period (delay and response), with subject as the repeated measure (Fig. 2b).

We also statistically compared these differential activity levels by performing ANOVAs on representative signals from each period (delay and response) in each differential time course (manipulation→maintenance and action→non-action), again with subject as the repeated measure (Fig. 3b).

Specify type of analysis: Whole brain ROI-based Both

Anatomical location(s)

A region of interest (ROI) in the left dlPFC was defined for each participant. The approximate location of the ROI was taken from the 6-minute functional localizer data following GLM analysis with FSL FEAT (Version 5.98). For the complete FEAT design protocol, please see (https://github.com/layerfMRI/repository/tree/master/DLPFC_Emily/Featdesign). The ROI was manually selected and drawn for every individual participant (see Fig. S3 for drawn ROIs in every participant scanned using the axial readout protocol).

Statistic type for inference
(See [Eklund et al. 2016](#))

No voxelwise inference was performed, therefore no correction for multiple comparisons was applied.

For Fig. 1c (post-hoc visualization taken from the functional localizer), we used a voxelwise p-value threshold of 0.01. Note that no statistical inference is performed on this data; the analysis was performed post-hoc simply for convenience of displaying the approximate macroscale ROI location across subjects. All statistical inference is performed on timecourse data extracted from single-subject space.

Correction

No voxelwise inference was performed, therefore no correction for multiple comparisons was applied.

Models & analysis

n/a | Involved in the study

- Functional and/or effective connectivity
- Graph analysis
- Multivariate modeling or predictive analysis